



Enabling efficient electrocatalytic conversion of N₂ to NH₃ by Ti₃C₂ MXene loaded with semi-metallic 1T'-MoS₂ nanosheets

Xiaoyue Chen^a, Songge Zhang^a, Xiu Qian^a, Zhangqian Liang^a, Yanjun Xue^a, Xiaoli Zhang^d, Jian Tian^{a,b,*}, Ye Han^{a,**}, Minhua Shao^{b,c,*}

^a School of Materials Science and Engineering, Shandong University of Science and Technology, Qingdao 266590, China

^b Department of Chemical and Biological Engineering, The Hong Kong University of Science and Technology, Clear Water Bay, Kowloon, Hong Kong, China

^c Energy Institute, and Chinese National Engineering Research Center for Control & Treatment of Heavy Metal Pollution, The Hong Kong University of Science and Technology, Clear Water Bay, Kowloon, Hong Kong, China

^d School of Materials Science and Engineering, Zhengzhou University, Zhengzhou 450001, China

ARTICLE INFO

Keywords:

Ti₃C₂ MXene

MoS₂

Semi-metallic 1T' phase

Electrocatalytic nitrogen fixation

ABSTRACT

Herein, we assemble semi-metallic 1T' phase MoS₂ on the surface Ti₃C₂ MXene (1T'-MoS₂/Ti₃C₂ composite) by one-step hydrothermal method for nitrogen fixation. 1T'-MoS₂/Ti₃C₂ composites present a high ammonia yield rate of 31.96 μg h⁻¹ mg⁻¹_{cat} at -0.95 V vs. RHE and a Faradaic efficiency (FE) of 30.75% at -0.7 V, which is much better than pure 1T'-MoS₂ and pure Ti₃C₂ MXenes alone. Furthermore, the 1T'-MoS₂/Ti₃C₂ composites exhibit good selectivity and stability with no significant decrease in ammonia yield rate and FE. Density functional theory (DFT) calculations reveal that 1T'-MoS₂/Ti₃C₂ composite makes the activation and further reduction of *N₂ more thermodynamically favorable than pure 1T'-MoS₂. ¹⁵N isotopic labeling experiment confirms that nitrogen in produced ammonia originates from N₂ in the electrolyte.

1. Introduction

Ammonia (NH₃), as one of important chemical substances, is mainly produced by the traditional Haber-Bosch process [1,2]. Due to the high energy consumption and large amounts of greenhouse gas emissions of Haber-Bosch technology, pursuing a sustainable and green NH₃ production strategy is urgent [3–5]. Using renewable electricity, electrocatalytic synthesis of NH₃ directly from nitrogen and water (N₂+3H₂O→2NH₃+3/2O₂) has become an attractive and important topic [2,6]. In the electrochemical nitrogen reduction reaction (NRR) [1,7–9], only water, N₂ (which can be replaced by air) and electricity are needed to make NH₃ [9]. The catalysts have become the core components of the electrocatalytic NRR system. Noble metals (including Ru, Rh and Au,) are extensively used as NRR electrocatalysts due to their strong bonding for a variety of reactants and excellent electrical conductivity. For example, electrodeposited Ru on carbon felt produced NH₃ from nitrogen and water achieves a rate of 0.21 × 10⁻⁶ g cm⁻² h⁻¹ [10]. Yet, the high cost and scarcity of noble metals restrict the practical application. Consequently, developing non-noble metal electrocatalysts is needed.

Inspired by biological nitrogen fixation [11–20], some Mo-based

catalysts (including Mo monatomic [21,22], sulfide [23–26], nitride [27,28], and carbides [29,30]) have been considered promising candidates for N₂ activation. Among them, MoS₂ has a structure similar to that of natural nitrogenase [31]. Nevertheless, most of the reported MoS₂ are 2H phase. Different from the semi-open edge configuration that is active for NRR, the base surface of 2H-MoS₂ is a sulfur-modified structure, showing poor catalytic activity [32,33]. Sun's group reported that 2H-MoS₂ presents good NRR performance in a 0.1 M Na₂SO₄ solution with a poor Faraday efficiency of only 1.17% [25]. Since metallic 1T-MoS₂ possesses more exposed active sites and better conductivity than 2H-MoS₂, the electrocatalytic NRR activity of 1T-MoS₂ is better than 2H-MoS₂ [34,35]. The semi-metallic 1T'-MoS₂, as a derivative of 1T-MoS₂, not only retains the excellent conductivity and abundant exposed base/edge active sites of 1T-MoS₂, but also has good stability, whose NRR property is not studied. As an emerging 2D material, Ti₃C₂ MXene is usually prepared by selectively etching the Al element from Ti₃AlC₂ [36–39]. Ti₃C₂ MXene has a broad prospect in the field of catalysis owing to the high specific surface area and high conductivity [40]. Wang's group reported that Ti₃C₂ MXenes present a relatively high Faraday efficiency (5.78%) for NRR [41].

* Corresponding authors at: School of Materials Science and Engineering, Shandong University of Science and Technology, Qingdao 266590, China.

** Corresponding author.

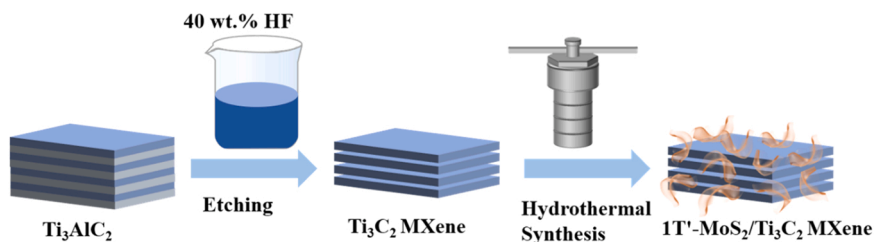
E-mail addresses: jiantian@sdust.edu.cn (J. Tian), hanye@sdust.edu.cn (Y. Han), kemshao@ust.hk (M. Shao).

<https://doi.org/10.1016/j.apcatb.2022.121277>

Received 3 July 2021; Received in revised form 28 February 2022; Accepted 1 March 2022

Available online 3 March 2022

0926-3373/© 2022 Elsevier B.V. All rights reserved.



Scheme 1. Schematic diagram of the preparation process for 1T'-MoS₂/Ti₃C₂ composites.

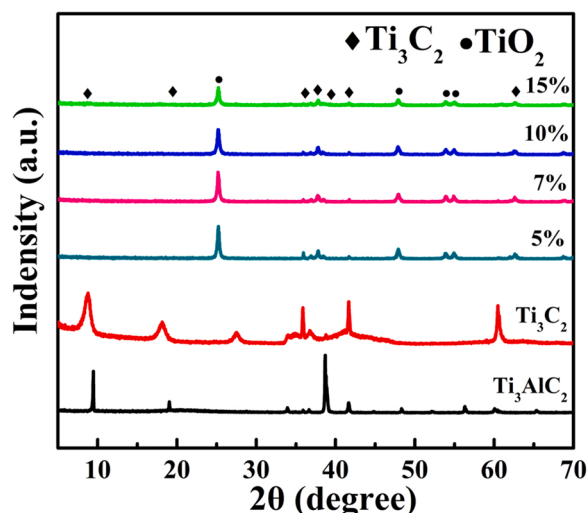


Fig. 1. XRD patterns of bulk Ti₃AlC₂, Ti₃C₂ MXene and 1T'-MoS₂/Ti₃C₂ composites with various loading of 1T'-MoS₂ nanosheets (5, 7, 10 and 15 wt% 1T'-MoS₂).

Herein, we constructed 1T'-MoS₂/Ti₃C₂ composites for electro-catalytic NRR, in which Ti₃C₂ MXene is a perfect support for loading 1T'-MoS₂ nanosheets. The 1T'-MoS₂/Ti₃C₂ composite presents good NRR activity with an average ammonia yield rate of 31.96 μg h⁻¹mg⁻¹_{cat.} at -0.95 V vs. RHE, and the highest Faraday efficiency of 30.75% at -0.7 V. Furthermore, the 1T'-MoS₂/Ti₃C₂ composite shows excellent selectivity and stability on NH₃. DFT calculations reveal that 1T'-MoS₂/Ti₃C₂ composite makes the activation and further reduction of *N₂ more thermodynamically favorable than pure 1T'-MoS₂.

2. Experimental section

2.1. Chemicals

The Ti₃AlC₂ powders were procured from 11 Technology Co., Ltd., Changchun. Hydrofluoric acid (HF, 40 wt%) and sodium hydroxide (NaOH) were procured from Yantai Yuandong Fine Biochemical Co., Ltd. Ethanol (C₂H₅OH), sodium sulfate anhydrous (Na₂SO₄) and ammonium tetrathiomolybdate ((NH₄)₂MoS₄) were procured from Shanghai Aladdin Biochemical Co., Ltd. Sodium nitroferrocyanide (III) dihydrate (Na₂[Fe(NO)(CN)₅]·2H₂O) and P-Dimethylaminobenzaldehyde (p-C₆H₄NO) were gained from Shanghai Macklin Biochemical Co., Ltd. Molybdenum trioxide (MoO₃), potassium thiocyanate (KSCN), hydrazine (N₂H₄·H₂O, 85 wt%), ammonium chloride (NH₄Cl), sulfuric acid (H₂SO₄, 98 wt%), hydrochloric acid (HCl, 36 wt%), salicylic acid (C₇H₆O₃), sodium hypochlorite (NaClO, 30 wt%) and sodium citrate (C₆H₅Na₃O₇) were procured from Sinopharm. Nafion solution (D520, 5 wt%) was acquired from Shanghai Hesen electric Co., Ltd.

2.2. Synthesis of Ti₃C₂ MXene nanosheets (NSs)

Ti₃C₂ MXene NSs were synthesized by HF etching. 3 g Ti₃AlC₂ powders were dissolved in HF solution (360 mL 40 wt%). The mixture was stirred at room temperature for 72 h, and was then washed. The lower layer of powder was collected while the supernatant was discarded. Finally, the obtained samples were Ti₃C₂ MXene NSs with Al layers removed and were dried in a vacuum oven.

2.3. Synthesis of 1T'-MoS₂ nanosheets/Ti₃C₂ MXene (1T'-MoS₂/Ti₃C₂) composites

1T'-MoS₂/Ti₃C₂ composites were prepared by the hydrothermal reaction. 32.5 mg (NH₄)₂MoS₄ was dissolved in 10 mL deionized water. Subsequently, 200 mg Ti₃C₂ MXene NSs were added to the above solution. The mixtures were stirred and treated by ultrasonic to form a uniformly dispersed suspension. Then the suspension was hydrothermally treated at 200 °C for 12 h. The obtained 1T'-MoS₂/Ti₃C₂ composites (10 wt% 1T'-MoS₂) were washed several times with deionized water and ethanol, respectively, and dried in a vacuum oven. Similarly, by modifying the mass of (NH₄)₂MoS₄ (16.3 mg, 22.8 mg and 48.8 mg), 1T'-MoS₂/Ti₃C₂ composites with other MoS₂ adding amounts (5 wt%, 7 wt% and 15 wt%) were prepared.

2.4. Preparation of 1T-MoS₂ nanosheets/Ti₃C₂ MXene (1T-MoS₂/Ti₃C₂) and 2H-MoS₂ nanosheets/Ti₃C₂ MXene (2H-MoS₂/Ti₃C₂) composites

6 mg MoO₃ and 8.09 mg KSCN were added to 30 mL deionized water. Subsequently, 60 mg Ti₃C₂ MXene nanosheets were dissolved in the above solution. The mixed solution was stirred by magnetic force and treated by ultrasonic to form a uniformly dispersed suspension. Then the suspension was hydrothermally treated at 200 °C for 12 h. The obtained 1T-MoS₂/Ti₃C₂ composites (10 wt% 1T-MoS₂) were washed several times with deionized water and ethanol, respectively, and dried in a vacuum oven.

To obtain 2H-MoS₂/Ti₃C₂ composites, the as-prepared 1T'-MoS₂/Ti₃C₂ composites were annealed in the Ar atmosphere and maintained at 400 °C for 2 h.

2.5. Characterizations

The XRD patterns of the catalysts were tested by a D/Max 2500PC diffractometer. The X-ray photoelectron spectrometry (XPS) spectra of the catalysts were executed on a Thermo Scientific K-Alpha (USA) spectrometer. The nanostructures of the products were observed by FEI Nova NanoSEM 450 high resolution scanning electron microscope (FESEM) equipped with energy dispersive spectroscopy (EDS) and Thermo Fisher Talos F200X high-resolution transmission electron microscope (HRTEM). The optical absorption spectra of the catalysts were measured on Agilent CARY 60 UV-Vis spectrophotometer. ¹H nuclear magnetic resonance (NMR) spectra were tested by a JNM-ECZ400S nuclear magnetic resonance spectrometer.

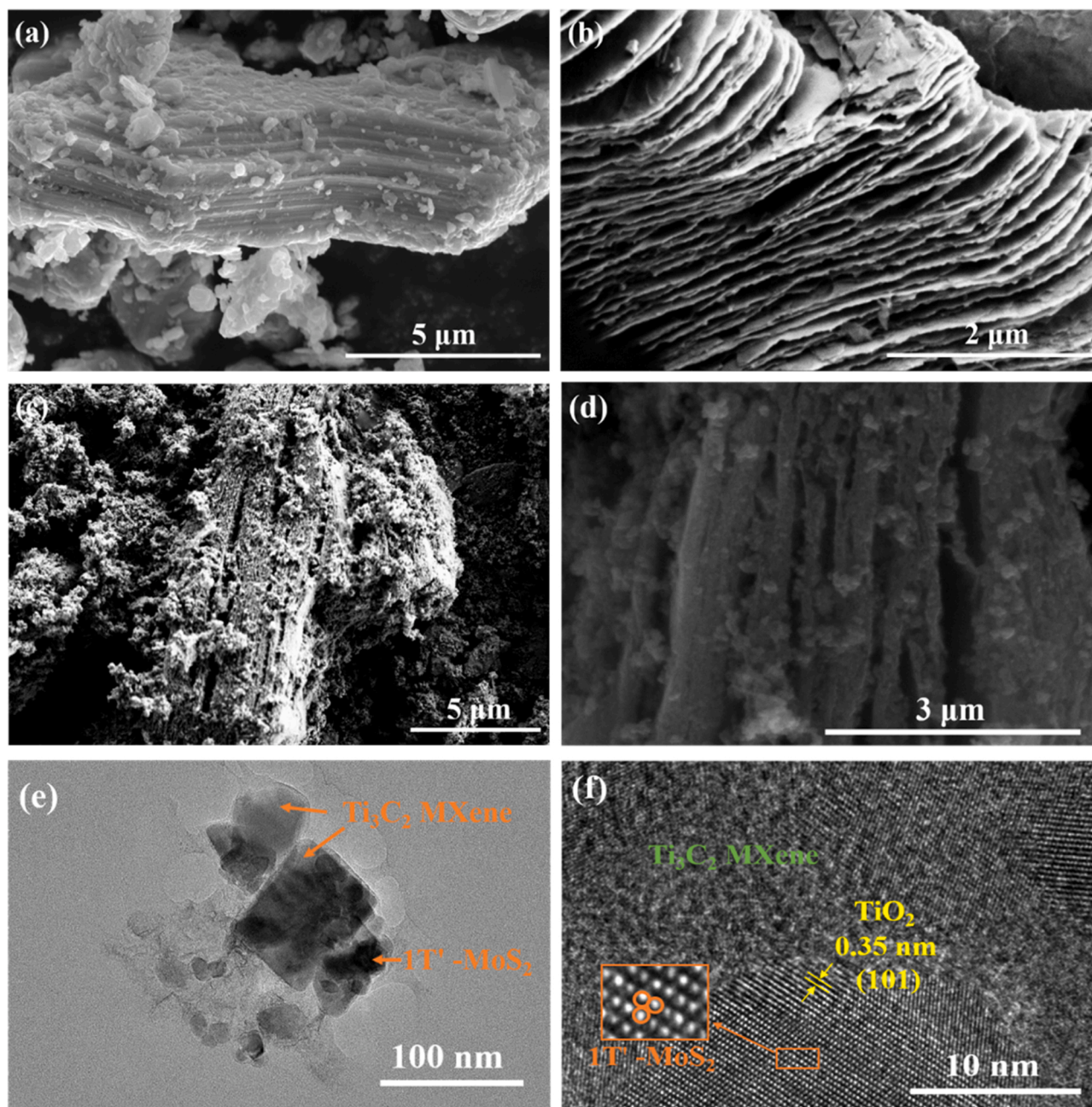


Fig. 2. SEM images of (a) Ti_3AlC_2 , (b) Ti_3C_2 MXene and (c, d) $1\text{T}'\text{-MoS}_2/\text{Ti}_3\text{C}_2$ composites (10 wt% $1\text{T}'\text{-MoS}_2$), respectively; (e) TEM images of $1\text{T}'\text{-MoS}_2/\text{Ti}_3\text{C}_2$ composites (10 wt% $1\text{T}'\text{-MoS}_2$); (f) HRTEM images of $1\text{T}'\text{-MoS}_2/\text{Ti}_3\text{C}_2$ composites (10 wt% $1\text{T}'\text{-MoS}_2$).

2.6. Electrochemical measurements

The electrochemical experiments in this study were performed in a typical H-type cell. The cathode and the anode chambers were separated by a Nafion 117 membrane. Before the NRR test, the membrane was heated in DI water for 1 h, followed by 5 wt% H_2O_2 , 0.5 M H_2SO_4 and DI water for 1 h at 80 $^\circ\text{C}$, to remove organic impurities and protonize the Nafion membrane. The electrochemical experiment was tested in a CHI 660E electrochemical workstation with a three-electrode system with the graphite rod and Ag/AgCl as the counter and reference electrodes. Before the test, the electrolyte needed to be purged with N_2 for 30 min. In addition, the electrocatalyst was also required to undergo potential cycling at a scanning rate of 100 mV s^{-1} for 50 cycles (0 to -0.8 V). The linear sweep voltammetry (LSV) test was performed at room temperature with a scan rate of 5 mV s^{-1} . During the experiment, high-purified

N_2 (purify: 99.999%) was pre-purified through a saturator equipped with 0.1 M KOH and 0.05 M H_2SO_4 to remove any possible impurities, such as NH_3 or NO_x , and then was continuously fed into the cathode chamber (constant flow rate: 20 mL min^{-1}) through a gas flow meter controlled. In addition, an online acid trap (a saturator equipped with 0.001 M H_2SO_4) was fixed at the cathode chamber's gas outlet to minimize the influence of the external environment or NH_3 escape on the quantitative results.

2.7. Determination of NH_3

The indophenol blue method was used to determine the concentration of NH_3 contained in the electrolyte by using a spectrophotometer. The electrolyte solution (2 mL) was extracted from the cathode chamber of the H-type electrolytic cell. Then, the NaOH (2 mL 1.0 M) containing

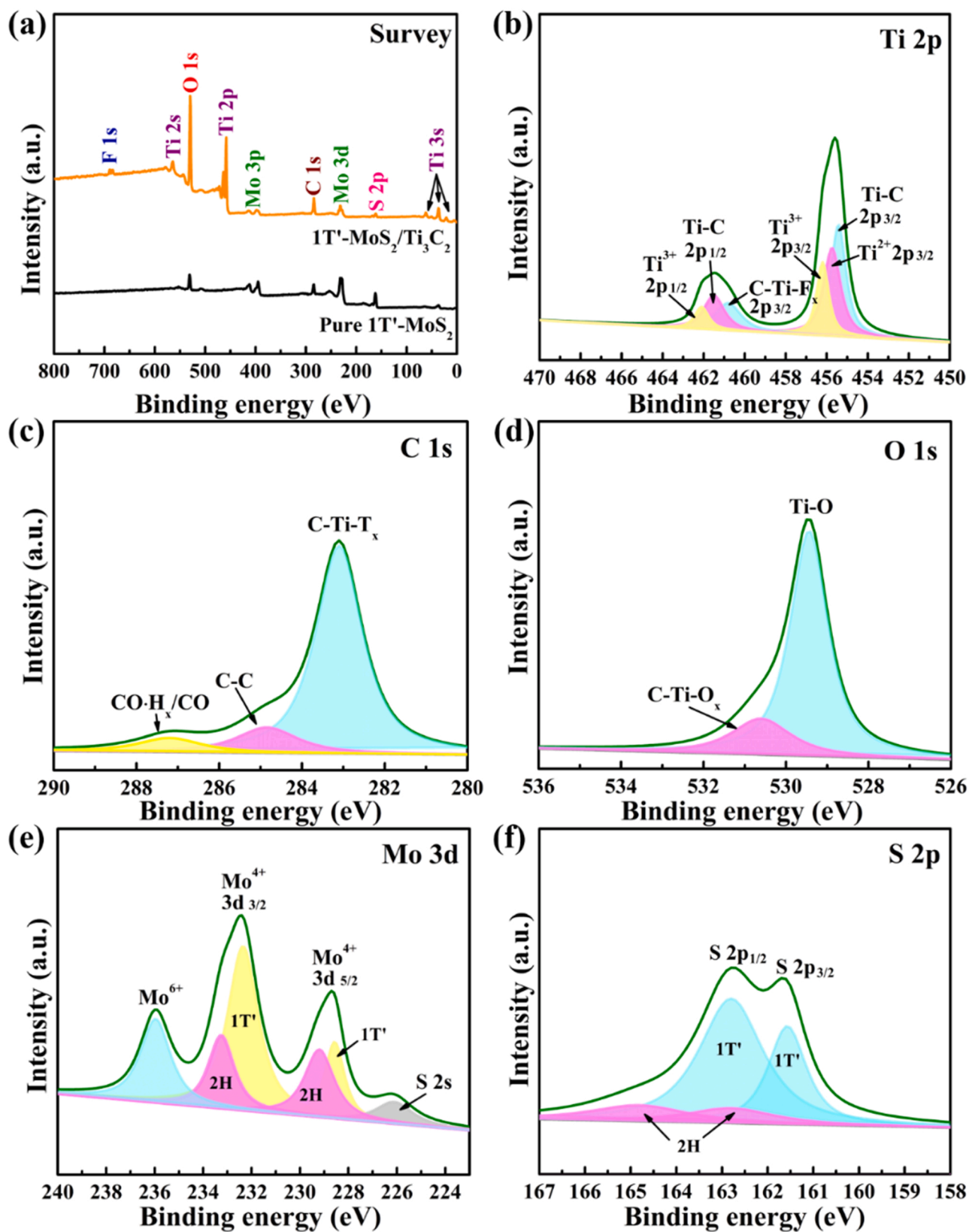


Fig. 3. (a) Survey XPS spectrum of pure 1T'-MoS₂ and 1T'-MoS₂/Ti₃C₂ composites (10 wt% 1T'-MoS₂); (b) Ti 2p, (c) C 1s, (d) O 1s, (e) Mo 3d and (f) S 2p XPS spectra of 1T'-MoS₂/Ti₃C₂ composites (10 wt% 1T'-MoS₂).

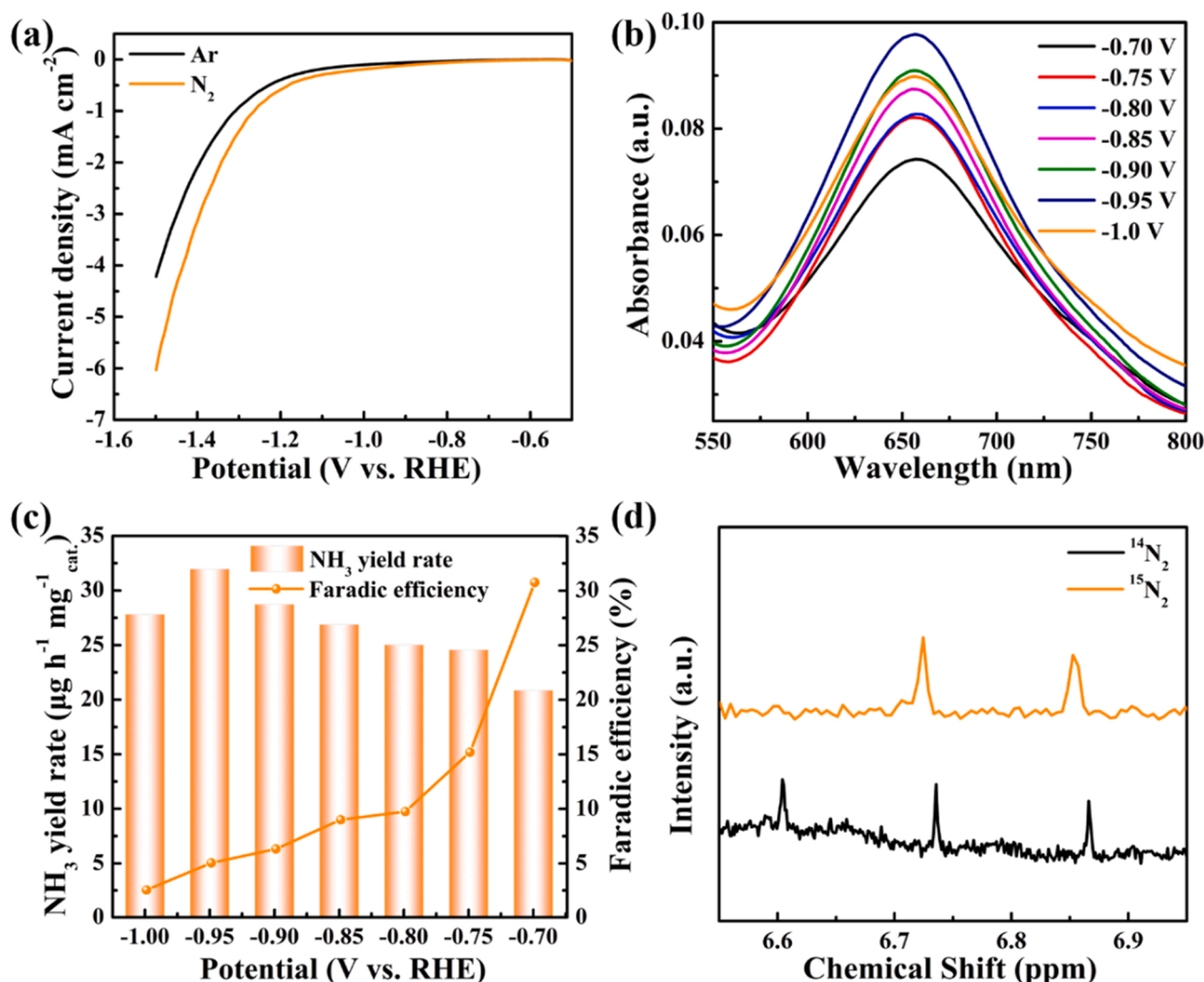


Fig. 4. (a) Linear sweep voltammetry (LSV) curves of 10 wt% 1T'-MoS₂/Ti₃C₂ composite materials recorded in N₂-saturated (orange line) and Ar-saturated (black line) 0.1 M Na₂SO₄. (b) UV-vis absorption spectra of 0.1 M Na₂SO₄ electrolyte after NRR for 1T'-MoS₂/Ti₃C₂ composites (10 wt% 1T'-MoS₂) at a series of potentials for 2H. (c) NH₃ yield rates and FEs of 1T'-MoS₂/Ti₃C₂ composites (10 wt% 1T'-MoS₂) at a series of potentials. (d) ¹H NMR spectra (400 MHz) of both ¹⁵NH₄⁺ and ¹⁴NH₄⁺ produced from the electrocatalysis using ¹⁵N₂ and ¹⁴N₂ as the feeding gas.

5 wt% sodium citrate and 5 wt% salicylic acid, NaClO (1 mL 0.05 M) and Na₂[Fe(NO)(CN)₅]·2H₂O (0.2 mL of 1 wt%) solution were successively added. The absorbance at 655 nm was applied to determine the concentration of NH₃.

2.8. Determination of N₂H₄

N₂H₄ in the electrolyte was estimated by Watt and Chrisp method. Firstly, C₂H₅OH (300 mL), HCl (30 mL) and P-C₉H₁₁NO (5.99 g) were mixed, stirred, and applied as a developer. The electrolyte (5 mL) was taken from the cathode chamber of the H-type electrolytic cell and added into 5 mL above solution. After standing for 10 min, the absorbance at 455 nm was applied to determine the concentration of N₂H₄.

2.9. Density functional theory (DFT) calculation

DFT calculations were tested using the Vienna Ab initio Simulation Package (VASP) [42,43]. The interactions between valence and core electrons were performed using the projector-augmented wave (PAW) method [44]. the force tolerance was 0.02 eV/Å and the total energy tolerance was 1×10^{-5} eV. The electronic occupancies were performed using Gaussian smearing with a smearing width of 0.20 eV. The pristine

Ti₃C₂ surface was modeled as a slab with 1-layered (3 × 3) unit cells of Ti₃C₂ (001) and 20 Å vacuum, where the bottom 3 atom-layers were fixed and the top 2 atom-layers were fully relaxed. The 1T'-MoS₂/Ti₃C₂ surface was modeled as a slab with 1-layered 1T'-MoS₂ [45] on top of 1-layered Ti₃C₂. A vacuum layer of 20 Å was applied to prohibit the periodic interactions of the slab. A $5 \times 5 \times 1$ Monkhorst-Pack k-point mesh was applied. Additionally, dipole corrections were added along with the z-direction, and van der Waals (vdW) corrections were calculated by the zero damping DFT-D3 method of Grimme [46,47].

3. Results and discussion

3.1. Catalyst synthesis, morphologies and structures

Scheme 1 presents the preparation process of the 1T'-MoS₂/Ti₃C₂ composites. Firstly, Ti₃AlC₂ MAX was etched by 40 wt% HF to eliminate the Al layers to obtain Ti₃C₂ MXene. Then, the resulting Ti₃C₂ MXene and (NH₄)₂MoS₄ were dispersed in the solution and hydrothermally treated at 200 °C for 12H to introduce 1T'-MoS₂ nanosheets, that are anchored on Ti₃C₂ MXene to form 1T'-MoS₂/Ti₃C₂ composites.

The crystalline phase of the samples was investigated by XRD (Fig. 1). The Ti₃AlC₂ MAX phase (black line) manifests excellent

Table 1

Comparison of the NRR performance of 1T'-MoS₂/Ti₃C₂ composite and other electrocatalysts.

Catalyst	Electrolyte	NH ₃ Yield Rate	Faradic Efficiency	Reference
1T'-MoS ₂ /Ti ₃ C ₂	0.1 M Na ₂ SO ₄	31.96 μg h ⁻¹ mg ⁻¹ _{cat.}	30.75%	This work
MoS ₂ /rGO	0.5 M Li ₂ ClO ₄	24.82 μg h ⁻¹ mg ⁻¹ _{cat.}	4.58%	[17]
DR-MoS ₂	0.1 M Na ₂ SO ₄	29.28 μg h ⁻¹ mg ⁻¹ _{cat.}	8.34%	[18]
Mo ₂ C/C	0.5 M Li ₂ SO ₄	11.30 μg h ⁻¹ mg ⁻¹ _{cat.}	7.8%	[29]
MoO ₃	0.1 M HCl	29.43 μg h ⁻¹ mg ⁻¹ _{cat.}	1.9%	[62]
Fe ₂ (MoO ₄) ₃	0.1 M Na ₂ SO ₄	7.5 μg h ⁻¹ mg ⁻¹ _{cat.}	1.0%	[65]
Vo-MoO ₂ /C	0.1 M Na ₂ SO ₄	9.75 μg h ⁻¹ mg ⁻¹ _{cat.}	3.24%	[66]
Mo-FeP	0.1 M HCl	13.1 μg h ⁻¹ mg ⁻¹ _{cat.}	7.49%	[67]
Ru SAs/Ti ₃ C ₂ O	0.1 M HCl	27.56 μg h ⁻¹ mg ⁻¹ _{cat.}	23.3%	[68]
CoS/S-MAs (Ti ₃ C ₂ T _x MXene)	0.1 M Na ₂ SO ₄	12.4 μg h ⁻¹ mg ⁻¹ _{cat.}	27.05%	[69]
1T'-MoS ₂ /Ti ₃ C ₂	0.1 M HCl	23.21 μg h ⁻¹ mg ⁻¹ _{cat.}	10.16%	[70]
SA Ru/Mo ₂ CT _x	0.5 M K ₂ SO ₄	40.57 μg h ⁻¹ mg ⁻¹ _{cat.}	25.77%	[71]
MoO _{3-x} /MXene	0.5 M LiClO ₄	95.8 μg h ⁻¹ mg ⁻¹ _{cat.}	22.3%	[72]

crystallinity, which is assigned to Ti₃AlC₂ [39,48]. After HF etching, the most intense (104) diffraction peak of Ti₃AlC₂ at 39° disappeared entirely (red line), and the (002) peak at 9.52° and (004) peak at 19.15° were broadened and deviated to low angles, indicating the successful transformation from Ti₃AlC₂ to Ti₃C₂ MXene [48,49]. The removal of Al layers resulted in the expansion of crystal plane spacing of Ti₃C₂ MXene. For the 1T'-MoS₂/Ti₃C₂ composites, the signal assigning to 1T'-MoS₂ (Fig. S1) was not detected, due to the ultra-thin and highly dispersed nature of 1T'-MoS₂ nanosheets [48]. In addition, the appearance of TiO₂ diffraction peaks in 1T'-MoS₂/Ti₃C₂ composites was attributed to the surface oxidation of Ti₃C₂ MXene [35].

The morphology of the catalysts was characterized by SEM (Fig. 2 and S2). Ti₃AlC₂ (Fig. 2a) presents a typical bulk morphology with a layered texture. The Al layers of Ti₃AlC₂ were removed after HF etching (Fig. 2b), and the bulk structure of the MAX is changed into an MXene layered structure, suggesting the successful formation of Ti₃C₂ MXene [39]. After MoS₂ was loaded on the Ti₃C₂ MXene via hydrothermal reaction, the smooth surface became rough and was covered by fine particles (Fig. 2c and S2a-c). In Fig. 2c, the particles on Ti₃C₂ MXene were further magnified and showed a sheet-like pure 1T'-MoS₂ morphology (Fig. 2d and S2d) [50]. In addition, EDS mapping images of 1T'-MoS₂/Ti₃C₂ composites suggest that MoS₂ is uniformly assembled on Ti₃C₂ MXene (Fig. S3).

The TEM image in Fig. 2e showed that Ti₃C₂ MXene was covered by a layer of uniform 1T'-MoS₂ nanosheets. Fig. 2f further illustrated that lattice fringes of 1T'-MoS₂ nanosheets and Ti₃C₂ MXene were staggered [51]. A typical triangle-like arrangement of Mo atoms in the base surface of MoS₂ demonstrates the existence of 1T'-MoS₂ [35]. In addition, the presence of TiO₂ was found at the edges. The lattice fringes with a spacing of 0.35 nm corresponded to the (101) crystal plane of TiO₂ [39]. The semiconductor property of TiO₂ in the 1T'-MoS₂/Ti₃C₂ composite can limit the transfer of electrons to a certain extent, and inhibit the HER reaction, which is beneficial to the NRR process [52].

The survey spectrum of 1T'-MoS₂/Ti₃C₂ composites (curve orange in Fig. 3a) confirms the existence of Ti, O, C, Mo and S elements. Due to the use of HF in the process of etching Ti₃C₂ MXene, F⁻ was physically

adsorbed onto Ti₃C₂ as a functional group, so the presence of a small amount of F element was also detected [48]. For the Ti 2p spectrum (Fig. 3b), the peaks at the binding energies of ~461.50 eV (Ti 2p_{1/2}) and ~455.46 eV (Ti 2p_{3/2}) can be ascribed to the Ti-C bond in Ti₃C₂ MXene [53,54]. The other three peaks at ~455.77 eV, ~456.26 eV and ~462.13 eV can be assigned to Ti²⁺ and Ti³⁺ of TiC or Ti₃C₂ in MXene, which are consistent with previous reports [53,55]. The remaining peak at ~460.62 eV belongs to C-Ti-F_x [53,55,56]. For the C 1s spectrum (Fig. 3c), three distinct peaks at ~283.06 eV, ~284.8 eV and ~287.11 eV are assigned to C-Ti-T_x, C-C and CO-H_x/CO bonds, mainly due to the influence of Ti₃C₂ and amorphous carbon [53,54,57]. For the O 1s spectrum (Fig. 3d), two peaks at ~529.53 eV and ~530.72 eV are attributed to Ti-O and C-Ti-O_x bonds, respectively [58]. Mo 3d and S 2p XPS spectra can further confirm the existence of 1T' phase MoS₂ in the composite. As shown in Fig. 3e, the main peaks at ~232.32 eV and ~228.52 eV are ascribed to Mo 3d_{3/2} and Mo 3d_{5/2} of 1T' phase MoS₂ [50,59]. The small peaks at ~233.28 eV and ~229.36 eV are attributed to Mo 3d_{3/2} and Mo 3d_{5/2} of 2H phase MoS₂ [60,61]. Moreover, an additional peak of Mo⁶⁺ belongs to MoO₃ at ~235.91 eV [62]. In the same way, two dominant peaks (Fig. 3f) in ~161.57 eV and ~162.78 eV are allocated to S 2p_{3/2} and S 2p_{1/2} of 1T' phase MoS₂ [50,59]. Besides, two small peaks at ~162.79 eV and ~164.82 eV are ascribed to S 2p_{3/2} and S 2p_{1/2} of 2H phase MoS₂ [60,61]. Mo 3d and S 2p XPS spectra (Fig. 3e and f) suggest the co-existence of 1T' and 2H phase in as-prepared 1T'-MoS₂/Ti₃C₂ composites, and 1T'-phase is the dominant phase (~73.45%, according to the peak area of XPS spectra). In addition, the presence of the peak at 400 eV corresponds to Mo 3p in the XPS survey (curve orange in Fig. 3a) [63].

3.2. Electrocatalytic nitrogen reduction reaction

Under the ambient condition, the electrocatalytic N₂ fixation was measured in the H-type electrolytic cell using the pretreated Nafion 117 as the separator. Since previous studies have shown that Nafion after pretreatment is one of the sources of ammonia pollution [64], we conducted a blank comparison experiment to prove that the N in the generated NH₄⁺ comes from N₂ in the electrolyte. In addition, an online acid trap (a saturator equipped with 0.001 M H₂SO₄) was installed at the cathode chamber's gas outlet to minimize the influence of the external environment or NH₃ escape on the quantitative results. The corresponding calibration curves of NH₄⁺ and N₂H₄ concentrations are shown in Fig. S4. An LSV test was carried out on 1T'-MoS₂/Ti₃C₂ composites in a 0.1 M Na₂SO₄ solution saturated with N₂ and Ar, respectively. In the N₂ saturated electrolyte (Fig. 4a), a higher current density can be clearly seen in the potential range of -0.7 to -1.5 V due to NRR. Next, the electrocatalytic performance of 1T'-MoS₂/Ti₃C₂ composites at -0.7 to -1.0 V was systematically studied (Fig. 4). Fig. 4b shows the absorbance curves of various electrolytes, indicating the NRR can occur in the potential range of -0.7 to -1.0 V. The average NH₃ yield rates and Faradaic efficiencies (FEs) within 2H at various potentials were tested (Fig. 4c). For 1T'-MoS₂/Ti₃C₂ composites (10 wt% 1T'-MoS₂), the ammonia yield presents a trend of increase first and then decrease with the potential becoming more negative. The maximum ammonia yield rate of 31.96 μg h⁻¹ mg⁻¹_{cat.} was realized at -0.95 V. The FE continued to decline with decreasing potential and the highest FE was 30.75% at -0.7 V. The obtained results suggest that our obtained 1T'-MoS₂/Ti₃C₂ composite is one of the best NRR electrocatalysts among Mo- and Ti₃C₂-based catalysts (Table 1).

By comparing the absorbance of the electrolyte before and after the reaction, no N₂H₄ was found, suggesting that the 1T'-MoS₂/Ti₃C₂ composites gave good selectivity (Fig. S5). Fig. S6a proves that no NH₃ was detected in the in-line acid trap, suggesting that all the produced NH₃ was dissolved in electrolyte with no escape. Furthermore, considering that a small amount of NO_x or NH₃ in the gas may exist, we measured the NH₃ content in 0.1 M Na₂SO₄ after N₂ is introduced for 30 min before the NRR test (Fig. S6b). NH₃ was not found, suggesting that the results

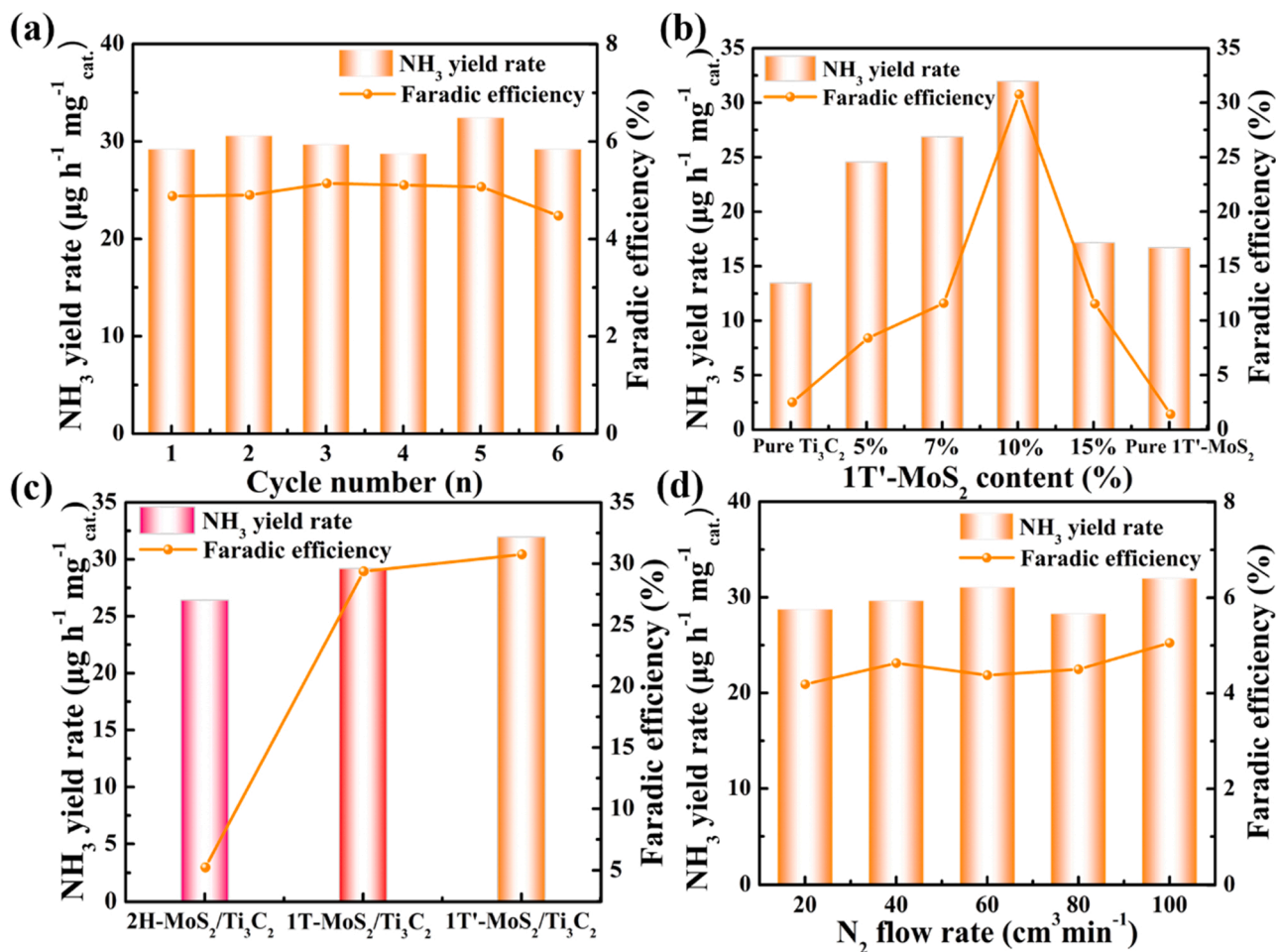


Fig. 5. (a) NH_3 yield rates and FEs of 10 wt% $1\text{T}'\text{-MoS}_2/\text{Ti}_3\text{C}_2$ composites at -0.95 V during recycling tests; (b) NH_3 yield rates and FEs of pure Ti_3C_2 MXene, pure $1\text{T}'\text{-MoS}_2$ and $1\text{T}'\text{-MoS}_2/\text{Ti}_3\text{C}_2$ composites with various content of $1\text{T}'\text{-MoS}_2$ (5, 7, 10 and 15 wt%) at -0.95 V; (c) NH_3 yield rates and FEs of $2\text{H-MoS}_2/\text{Ti}_3\text{C}_2$ composites, $1\text{T-MoS}_2/\text{Ti}_3\text{C}_2$ composites and $1\text{T}'\text{-MoS}_2/\text{Ti}_3\text{C}_2$ composites with same 10 wt% content of MoS_2 ; (d) NH_3 yield rates and FEs of $1\text{T}'\text{-MoS}_2/\text{Ti}_3\text{C}_2$ composites (10 wt% $1\text{T}'\text{-MoS}_2$) with different N_2 flow rates.

are not disturbed by possible impurities. Furthermore, to confirm that all the NH_3 in the cathode chamber in the experiment was produced by NRR, the NRR reaction was tested in the electrolyte saturated with Ar at -0.95 V vs. RHE and in the electrolyte saturated with N_2 at the open circuit potential, respectively. The UV-vis spectra under these two test conditions (Fig. S6c and d) show that NH_3 was not found, suggesting that all the previously produced NH_3 comes from electrocatalysis. ^1H nuclear magnetic resonance spectra (^1H NMR, Fig. 4d) present a doublet coupling for $^{15}\text{NH}_4^+$ and a triplet coupling for $^{14}\text{NH}_4^+$ with $^{15}\text{N}_2$ and $^{14}\text{N}_2$ as the N_2 source, respectively [28], which confirm that the produced NH_3 origin from the electrocatalytic conversion of N_2 .

In addition, cyclic and chronoamperometric currents were used to study the stability of catalysts, which is an important indicator for the performance evaluation of catalysts. Since the ammonia yield rate of the $1\text{T}'\text{-MoS}_2/\text{Ti}_3\text{C}_2$ composites reached a peak at -0.95 V, the durability of the catalysts was studied at this potential. Without changing the electrode and Nafion membrane, the electrolyte was replaced every hour and the concentration of NH_3 was tested. After 6 cycles (Fig. 5a), the ammonia yield rate and FE did not change significantly, suggesting that the $1\text{T}'\text{-MoS}_2/\text{Ti}_3\text{C}_2$ composites present good electrochemical stability. Moreover, at -0.95 V, the current density did not display a significant drop after 12h NRR test (Fig. S7a), demonstrating the catalyst's good durability. At the same time, the current density curves with time under different potentials show that the current density remains stable in the potential window of -0.7 to -1.0 V vs. RHE, which proves that the catalyst maintains good stability within this potential range (Fig. S7b).

In addition, we compared the phase and morphology of the catalysts after the reaction. As shown in Fig. S8a, XRD analysis shows that the crystalline phase of the $1\text{T}'\text{-MoS}_2/\text{Ti}_3\text{C}_2$ composites does not change significantly before and after the reaction. And the TEM image shows that the nanosheet features of the $1\text{T}'\text{-MoS}_2/\text{Ti}_3\text{C}_2$ composites are also preserved after NRR (Fig. S8b).

On the basis of the above experiments, the influence of $1\text{T}'\text{-MoS}_2$ adding amounts on NRR activity was studied. Notably, the ammonia yield rates of pure Ti_3C_2 MXene and pure $1\text{T}'\text{-MoS}_2$ are 13.46 and $16.70 \mu\text{g h}^{-1} \text{mg}^{-1}_{\text{cat}}$, and FEs are 2.51% and 1.40% , respectively, which is significantly lower than $1\text{T}'\text{-MoS}_2/\text{Ti}_3\text{C}_2$ composites ($31.96 \mu\text{g h}^{-1} \text{mg}^{-1}_{\text{cat}}$ and 30.75%). As the loading of $1\text{T}'\text{-MoS}_2$ increases (Fig. 5b), the ammonia yield rates and FEs show a trend of first rising and then falling, and reaching the peak value at 10 wt% loading amount. Furthermore, the NRR performance of $2\text{H-MoS}_2/\text{Ti}_3\text{C}_2$ composites, $1\text{T-MoS}_2/\text{Ti}_3\text{C}_2$ composites and $1\text{T}'\text{-MoS}_2/\text{Ti}_3\text{C}_2$ composites with the same 10 wt% MoS_2 were further compared (Fig. 5c). Remarkably, the ammonia yield rates of $2\text{H-MoS}_2/\text{Ti}_3\text{C}_2$ composites and $1\text{T-MoS}_2/\text{Ti}_3\text{C}_2$ composites are 26.41 and $29.18 \mu\text{g h}^{-1} \text{mg}^{-1}_{\text{cat}}$, and FEs are 5.23% and 29.37% , respectively, which is significantly lower than $1\text{T}'\text{-MoS}_2/\text{Ti}_3\text{C}_2$ composites ($31.96 \mu\text{g h}^{-1} \text{mg}^{-1}_{\text{cat}}$ and 30.75%). Furthermore, the NH_3 yield rates and FEs may be affected by other factors that have nothing to do with the catalyst itself, such as the flow rate of nitrogen gas. Therefore, we tested the NH_3 yield rates and FEs of $1\text{T}'\text{-MoS}_2/\text{Ti}_3\text{C}_2$ composites at different N_2 flow rates (Fig. 5d). The nitrogen fixation performance of the electrocatalyst was not affected by

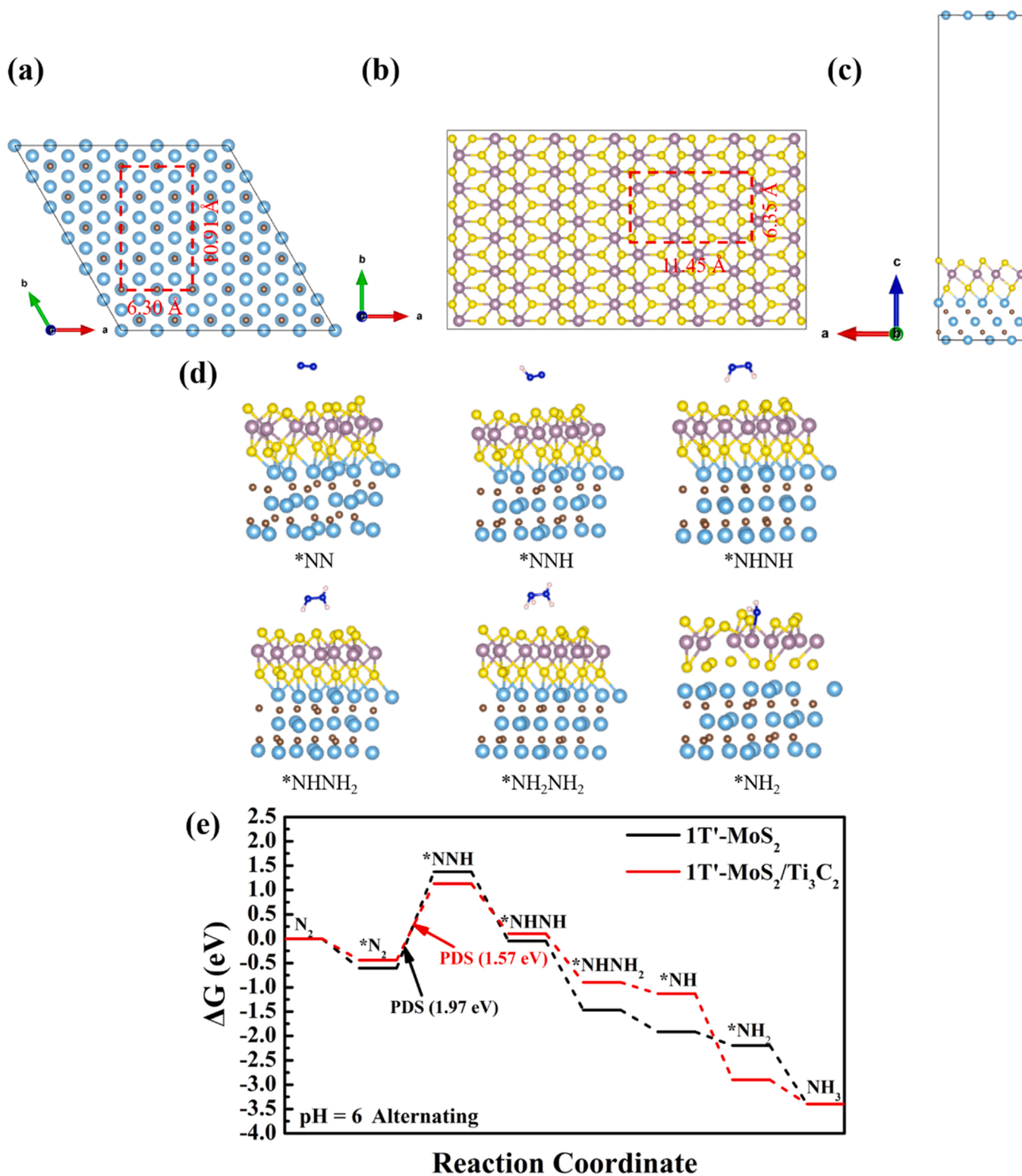


Fig. 6. The configuration of 1T'-MoS₂/Ti₃C₂ heterostructure: (a) the directions and lengths of the Ti₃C₂ slab, (b) the directions and lengths of the 1T'-MoS₂ slab, and (c) the model of 1T'-MoS₂/Ti₃C₂ (light blue-Ti, brown-C, plump-Mo, and yellow-S); (d) Most stable configurations of reaction intermediates on the surface of 1T'-MoS₂/Ti₃C₂ along the NRR alternating pathway (color notation: light blue-Ti, brown-C, plump-Mo, yellow-S, blue-N, and pink-H); (e) Gibbs free energy diagram of the NRR alternating pathway on the surface of 1T'-MoS₂ and 1T'-MoS₂/Ti₃C₂ at $U_{\text{RHE}} = -0.65 \text{ V}$ and pH = 6.

the modification of the gas flow rate.

3.3. DFT calculations

DFT calculations were measured to explore the origin of the

improved performance of 1T'-MoS₂/Ti₃C₂ toward NRR. The configuration of 1T'-MoS₂/Ti₃C₂ heterostructure was shown in Fig. 6a–d. The most stable configurations of reaction intermediates on the surface of 1T'-MoS₂/Ti₃C₂ and 1T'-MoS₂ are displayed in Fig. 6d and S9. The NRR performance is estimated by the Gibbs free energy diagram. The most

favorable reaction pathway is the alternating pathway for both structural models. For comparison, the distal pathway is also tested (Fig. S10). The reduction of *N_2 to *NNH is the potential-determining step (PDS) for both structural models (Fig. 6e). Nevertheless, the energy barrier for the reduction of *N_2 on the surface of $1T'-MoS_2/Ti_3C_2$ (1.57 eV) is lower than pure $1T'-MoS_2$ (1.97 eV), indicating that the $1T'-MoS_2/Ti_3C_2$ heterostructure makes the activation and further reduction of *N_2 more thermodynamically favorable than pure $1T'-MoS_2$.

4. Conclusions

In summary, we prepared $1T'-MoS_2/Ti_3C_2$ composites for NRR through assembling $1T'-MoS_2$ nanosheets on Ti_3C_2 MXenes' surface. In 0.1 M Na_2SO_4 , $1T'-MoS_2/Ti_3C_2$ composite catalyst reaches a high ammonia yield rate of $31.96 \mu g h^{-1} mg^{-1}_{cat}$ at -0.95 V and a high FEs of 30.75% at -0.7 V, better than pure $1T'-MoS_2$ and Ti_3C_2 MXene alone. $1T'-MoS_2/Ti_3C_2$ composite also exhibits remarkable selectivity and excellent chemical stability. ^{15}N isotopic labeling experiment reveals that the NH_4^+ comes from N_2 in the electrolyte. DFT calculations confirm that $1T'-MoS_2/Ti_3C_2$ composite makes the activation and further reduction of *N_2 more thermodynamically favorable than pure $1T'-MoS_2$. Our work presents a feasible way for the rational design and utilization of Mo-based NRR catalysts in the future.

CRediT authorship contribution statement

Xiaoyue Chen: Methodology, Visualization, Writing – original draft. **Songge Zhang:** Methodology, Visualization, Writing – review & editing. **Xiu Qian:** Formal analysis. **Zhangqian Liang:** Resources. **Yanjun Xue:** Funding acquisition. **Xiaoli Zhang:** Methodology, Writing – review & editing. **Jian Tian:** Methodology, Conceptualization, Supervision, Writing – original draft. **Ye Han:** Supervision, Writing – original draft. **Minhua Shao:** Methodology, Supervision, Writing – original draft.

Declaration of Competing Interest

The authors declare that they have no known competing financial interests or personal relationships that could have appeared to influence the work reported in this paper.

Acknowledgment

The authors are thankful for funding from the National Natural Science Foundation of China (No. 51872173), Hong Kong Scholars Program (No. XJ2019042), Innovation and Technology Commission of the Hong Kong Special Administrative Region (No. ITC-CNERC14EG03), Taishan Scholars Program of Shandong Province (No. tsqn201812068), Higher School Youth Innovation Team of Shandong Province (No. 2019KJA013), Science and Technology Special Project of Qingdao City (No. 20-3-4-3-nsh), the Opening Fund of State Key Laboratory of Heavy Oil Processing (No. SKLOP202002006). The authors would like to thank Shiyanjia Lab (www. Shiyanjia. Com) for the XPS analysis.

Appendix A. Supporting information

Supplementary data associated with this article can be found in the online version at [doi:10.1016/j.apcatb.2022.121277](https://doi.org/10.1016/j.apcatb.2022.121277).

References

- [1] C. Guo, J. Ran, A. Vasileff, S. Qiao, Rational design of electrocatalysts and photo (electro)catalysts for nitrogen reduction to ammonia (NH_3) under ambient conditions, *Energy Environ. Sci.* 11 (2018) 45–56, <https://doi.org/10.1039/C7EE02220D>.
- [2] C. Tang, S. Qiao, How to explore ambient electrocatalytic nitrogen reduction reliably and insightfully, *Chem. Soc. Rev.* 48 (2019) 3166–3180, <https://doi.org/10.1039/C9CS00280D>.
- [3] M. Kitano, Y. Inoue, Y. Yamazaki, F. Hayashi, S. Kanbara, S. Matsuishi, T. Yokoyama, S.W. Kim, M. Hara, H. Hosono, Ammonia synthesis using a stable electrode as an electron donor and reversible hydrogen store, *Nat. Chem.* 4 (2012) 934–940, <https://doi.org/10.1038/nchem.1476>.
- [4] T. Oshikiri, K. Ueno, H. Misawa, Selective dinitrogen conversion to ammonia using water and visible light through plasmon-induced charge separation, *Angew. Chem. Int. Ed.* 55 (2016) 3942–3946, <https://doi.org/10.1002/anie.201511189>.
- [5] C.J. van der Ham, M.T. Koper, D.G. Hetterscheid, D.G. Hetterscheid, Challenges in reduction of dinitrogen by proton and electron transfer, *Chem. Soc. Rev.* 43 (2014) 5183–5191, <https://doi.org/10.1039/C4CS00085D>.
- [6] L. Wang, M. Xia, H. Wang, K. Huang, C. Qian, C.T. Maravelias, G.A. Ozin, Greening ammonia toward the solar ammonia refinery, *Joule* 2 (2018) 1055–1074, <https://doi.org/10.1016/j.joule.2018.04.017>.
- [7] F. Zhou, L.M. Azofra, M. Ali, M. Kar, A.N. Simonov, C. McDonnell-Worth, C. Sun, X. Zhang, D.R. MacFarlane, Electro-synthesis of ammonia from nitrogen at ambient temperature and pressure in ionic liquids, *Energy Environ. Sci.* 10 (2017) 2516–2520, <https://doi.org/10.1039/C7EE02716H>.
- [8] M. Brian, D.R.D. Hoffman, Lance C. Seefeldt, Climbing nitrogenase toward a mechanism of enzymatic nitrogen fixation, *Acc. Chem. Res.* 42 (2009) 609–619, <https://doi.org/10.1021/ar8002128>.
- [9] R. Lan, J.T. Irvine, S. Tao, Synthesis of ammonia directly from air and water at ambient temperature and pressure, *Sci. Rep.* 3 (2013) 1145, <https://doi.org/10.1038/srep01145>.
- [10] V. Kordali, G. Kyriacou, C. Lambrou, Electrochemical synthesis of ammonia at atmospheric pressure and low temperature in a solid polymer electrolyte cell, *Chem. Commun.* 7 (2000) 1673–1674, <https://doi.org/10.1039/B004885M>.
- [11] Y. Wan, J. Xu, R. Lv, Heterogeneous electrocatalysts design for nitrogen reduction reaction under ambient conditions, *Mater. Today* 27 (2019) 69–90, <https://doi.org/10.1016/j.mattod.2019.03.002>.
- [12] B.M. Hoffman, D. Lukoyanov, Z.Y. Yang, D.R. Dean, L.C. Seefeldt, Mechanism of nitrogen fixation by nitrogenase: the next stage, *Chem. Rev.* 114 (2014) 4041–4062, <https://doi.org/10.1021/cr400641x>.
- [13] K. Michael, J.K. Chan, D.C. Rees, The nitrogenase FeMo-cofactor and P-cluster pair: 2.2 Å resolution structures, *Science* 260 (1993) 792–794, <https://doi.org/10.1126/science.8484118>.
- [14] K.M. Lancaster, M.R. Roemelt, P. Ettenhuber, Y. Hu, M.W. Ribbe, F. Neese, U. Bergmann, S. DeBeer, X-ray emission Spectroscopy evidences a central carbon in the nitrogenase iron-molybdenum cofactor, *Science* 334 (2011) 974–977, <https://doi.org/10.1126/science.1206445>.
- [15] H. Wang, Z. Li, Y. Li, B. Yang, J. Chen, L. Lei, S. Wang, Y. Hou, An exfoliated iron phosphorus trisulfide nanosheet with rich sulfur vacancy for efficient dinitrogen fixation and Zn- N_2 battery, *Nano Energy* 81 (2021), 105613, <https://doi.org/10.1016/j.nanoen.2020.105613>.
- [16] Y. Kong, Y. Li, X. Sang, B. Yang, Z. Li, S. Zheng, Q. Zhang, S. Yao, X. Yang, L. Lei, S. Zhou, G. Wu, Y. Hou, Atomically dispersed zinc(I) active sites to accelerate nitrogen reduction kinetics for ammonia electrosynthesis, *Adv. Mater.* 34 (2022) 2103548, <https://doi.org/10.1002/adma.202103548>.
- [17] Y. Li, J. Li, J. Huang, J. Chen, Y. Kong, B. Yang, Z. Li, L. Lei, G. Chai, Z. Wen, L. Dai, Y. Hou, Boosting electroreduction kinetics of nitrogen to ammonia via tuning electron distribution of single-atomic iron sites, *Angew. Chem. Int. Ed.* 60 (2021) 9078–9085, <https://doi.org/10.1002/anie.202100526>.
- [18] H. Wang, J. Si, T. Zhang, Y. Li, B. Yang, Z. Li, J. Chen, Z. Wen, C. Yuan, L. Lei, Y. Hou, Exfoliated metallic niobium disulfate nanosheets for enhanced electrochemical ammonia synthesis and Zn- N_2 battery, *Appl. Catal. B-Environ.* 270 (2020), 118892, <https://doi.org/10.1016/j.apcatb.2020.118892>.
- [19] Y. Liu, B. Huang, X. Chen, Z. Tian, X. Zhang, P. Tsiakaras, P. Shen, Electrocatalytic production of ammonia: Biomimetic electrode-electrolyte design for efficient electrocatalytic nitrogen fixation under ambient conditions, *Appl. Catal. B-Environ.* 271 (2020), 118919, <https://doi.org/10.1016/j.apcatb.2020.118919>.
- [20] Y. Liu, X. Zhang, Z. Chen, X. Zhang, P. Tsiakaras, P. Shen, Electrocatalytic reduction of nitrogen on FeAg/Si for ammonia synthesis: A simple strategy for continuous regulation of faradaic efficiency by controlling H^+ ions transfer rate, *Appl. Catal. B-Environ.* 283 (2021), 119606, <https://doi.org/10.1016/j.apcatb.2020.119606>.
- [21] L. Han, X. Liu, J. Chen, R. Lin, H. Liu, F. Lu, S. Bak, Z. Liang, S. Zhao, E. Stavitski, J. Luo, R.R. Adzic, H.L. Xin, Atomically dispersed molybdenum catalysts for efficient ambient nitrogen fixation, *Angew. Chem. Int. Ed.* 58 (2019) 2321–2325, <https://doi.org/10.1002/anie.201811728>.
- [22] L. Hui, Y. Xue, H. Yu, Y. Liu, Y. Fang, C. Xing, B. Huang, Y. Li, Highly efficient and selective generation of ammonia and hydrogen on a graphdiyne-based catalyst, *J. Am. Chem. Soc.* 141 (2019) 10677–10683, <https://doi.org/10.1021/jacs.9b03004>.
- [23] X. Li, X. Ren, X. Liu, J. Zhao, X. Sun, Y. Zhang, X. Kuang, T. Yan, Q. Wei, D. Wu, A MoS₂ nanosheet-reduced graphene oxide hybrid: an efficient electrocatalyst for electrocatalytic N₂ reduction to NH₃ under ambient conditions, *J. Mater. Chem. A* 7 (2019) 2524–2528, <https://doi.org/10.1039/C8TA10433F>.
- [24] X. Li, T. Li, Y. Ma, Q. Wei, W. Qiu, H. Guo, X. Shi, P. Zhang, A.M. Asiri, L. Chen, B. Tang, X. Sun, Boosted electrocatalytic N₂ reduction to NH₃ by defect-rich MoS₂ nanoflower, *Adv. Energy Mater.* 8 (2018) 1801357, <https://doi.org/10.1002/aenm.201801357>.
- [25] L. Zhang, X. Ji, X. Ren, Y. Ma, X. Shi, Z. Tian, A.M. Asiri, L. Chen, B. Tang, X. Sun, Electrochemical ammonia synthesis via nitrogen reduction reaction on a MoS₂ catalyst: theoretical and experimental studies, *Adv. Mater.* 30 (2018), e1800191, <https://doi.org/10.1002/adma.201800191>.

- [26] H. Su, L. Chen, Y. Chen, R. Si, Y. Wu, X. Wu, Z. Geng, W. Zhang, J. Zeng, Single atoms of iron on MoS₂ nanosheets for N₂ electroreduction into ammonia, *Angew. Chem. Int. Ed.* 59 (2020) 20411–20416, <https://doi.org/10.1002/anie.202009217>.
- [27] L. Zhang, X. Ji, X. Ren, Y. Luo, X. Shi, A.M. Asiri, B. Zheng, X. Sun, Efficient electrochemical N₂ reduction to NH₃ on MoN nanosheets array under ambient conditions, *ACS Sustain. Chem. Eng.* 6 (2018) 9550–9554, <https://doi.org/10.1021/acssuschemeng.8b01438>.
- [28] X. Ren, G. Cui, L. Chen, F. Xie, Q. Wei, Z. Tian, X. Sun, Electrochemical N₂ fixation to NH₃ under ambient conditions: Mo₃N nanorod as a highly efficient and selective catalyst, *Chem. Commun.* 54 (2018) 8474–8477, <https://doi.org/10.1039/C8CC03627F>.
- [29] H. Cheng, L. Ding, G. Chen, L. Zhang, J. Xue, H. Wang, Molybdenum carbide nanodots enable efficient electrocatalytic nitrogen fixation under ambient conditions, *Adv. Mater.* 30 (2018), e1803694, <https://doi.org/10.1002/adma.201803694>.
- [30] X. Ren, J. Zhao, Q. Wei, Y. Ma, H. Guo, Q. Liu, Y. Wang, G. Cui, A.M. Asiri, B. Li, B. Tang, X. Sun, High-performance N₂-to-NH₃ conversion electrocatalyzed by Mo₂C nanorod, *ACS Cent. Sci.* 5 (2019) 116–121, <https://doi.org/10.1021/acscentsci.8b00734>.
- [31] C.W. Huang, C.E. McKenna, In vivo reduction of cyclopropane by Azotobacter vinelandii nitrogenase, *Nature* 280 (1979) 609–611, <https://doi.org/10.1038/280609a0>.
- [32] W. Wu, C. Niu, C. Wei, Y. Jia, C. Li, Q. Xu, Activation of MoS₂ basal planes for hydrogen evolution by zinc, *Angew. Chem. Int. Ed.* 58 (2019) 2029–2033, <https://doi.org/10.1002/anie.201812475>.
- [33] T.F. Jaramillo, K.P. Jørgensen, J. Bonde, J.H. Nielsen, S. Hørch, I. Chorkendorff, Identification of active edge sites for electrochemical H₂ evolution from MoS₂ nanocatalysts, *Science* 317 (2007) 100–102, <https://doi.org/10.1002/anie.201812475>.
- [34] X. Chen, C. Ma, Z. Tan, X. Wang, X. Qian, X. Zhang, J. Tian, S. Yan, M. Shao, One-dimensional screw-like MoS₂ with oxygen partially replacing sulfur as an electrocatalyst for the N₂ reduction reaction, *Chem. Eng. J.* 433 (2022), 134504, <https://doi.org/10.1016/j.cej.2022.134504>.
- [35] X. Xu, X. Tian, B. Sun, Z. Liang, H. Cui, J. Tian, M. Shao, 1T-phase molybdenum sulfide nanodots enable efficient electrocatalytic nitrogen fixation under ambient conditions, *Appl. Catal. B-Environ.* 272 (2020), 118984, <https://doi.org/10.1016/j.apcatb.2020.118984>.
- [36] X. Liang, Y. Rangom, C.Y. Kwok, Q. Pang, L.F. Nazar, Interwoven MXene nanosheet/carbon-nanotube composites as Li-S cathode hosts, *Adv. Mater.* 29 (2017) 1603040, <https://doi.org/10.1002/adma.201603040>.
- [37] M. Liu, J. Li, R. Bian, X. Wang, Y. Ji, X. Zhang, J. Tian, F. Shi, H. Cui, ZnO@Ti₃C₂ MXene interfacial Schottky junction for boosting spatial charge separation in photocatalytic degradation, *J. Alloy. Compd.* 905 (2022), 164025, <https://doi.org/10.1016/j.jallcom.2022.164025>.
- [38] J. Zhao, L. Zhang, X. Xie, X. Li, Y. Ma, Q. Liu, W. Fang, X. Shi, G. Cui, X. Sun, Ti₃C₂X₂ (T = F, OH) MXene nanosheets: conductive 2D catalysts for ambient electrohydrogenation of N₂ to NH₃, *J. Mater. Chem. A* 6 (2018) 24031–24035, <https://doi.org/10.1039/C8TA09840A>.
- [39] B. Sun, P. Qiu, Z. Liang, Y. Xue, X. Zhang, L. Yang, H. Cui, J. Tian, The fabrication of 1D/2D CdS nanorod@Ti₃C₂ MXene composites for good photocatalytic activity of hydrogen generation and ammonia synthesis, *Chem. Eng. J.* 406 (2021), 127177, <https://doi.org/10.1016/j.cej.2020.127177>.
- [40] J. Lei, X. Zhang, Z. Zhou, Recent advances in MXene: preparation, properties, and applications, *Front. Phys.* 10 (2015) 276–286, <https://doi.org/10.1007/s11467-015-0493-x>.
- [41] Y. Luo, G. Chen, L. Ding, X. Chen, L. Ding, H. Wang, Efficient electrocatalytic N₂ fixation with MXene under ambient conditions, *Joule* 3 (2019) 279–289, <https://doi.org/10.1016/j.joule.2018.09.011>.
- [42] G. Kresse, J. Furthmüller, Efficient iterative schemes for ab initio total-energy calculations using a plane-wave basis set, *Phys. Rev. B Condens. Matter* 54 (1996) 11169–11186, <https://doi.org/10.1103/PhysRevB.54.11169>.
- [43] J.P. Perdew, K. Burke, M. Ernzerhof, Generalized gradient approximation made simple, *Phys. Rev. Lett.* 77 (1996) 3865–3868, <https://doi.org/10.1103/PhysRevLett.77.3865>.
- [44] P.E. Blöchl, Projector augmented-wave method, *Phys. Rev. B Condens. Matter* 50 (1994) 17953–17979, <https://doi.org/10.1103/PhysRevB.50.17953>.
- [45] X. Qian, J. Liu, L. Fu, J. Li, Quantum spin Hall effect in two-dimensional transition metal dichalcogenides, *Science* 346 (2014) 1344–1347, <https://doi.org/10.1126/science.1256815>.
- [46] S. Grimme, J. Antony, S. Ehrlich, H. Krieg, A consistent and accurate ab initio parametrization of density functional dispersion correction (DFT-D) for the 94 elements H–Pu, *J. Chem. Phys.* 132 (2010), 154104, <https://doi.org/10.1063/1.3382344>.
- [47] W.M. Haynes, *CRC Handbook of Chemistry and Physics: A Ready-reference Book of Chemical and Physical Data*, 97 ed., CRC Press, Boca Raton, FL, 2017.
- [48] X. Chen, Y. Guo, R. Bian, Y. Ji, X. Wang, X. Zhang, H. Cui, J. Tian, Titanium carbide MXenes coupled with cadmium sulfide nanosheets as two-dimensional/two-dimensional heterostructures for photocatalytic hydrogen production, *J. Colloid Interface Sci.* 613 (2022) 644–651, <https://doi.org/10.1016/j.jcis.2022.01.079>.
- [49] M. Naguib, M. Kurtoglu, V. Presser, J. Lu, J. Niu, M. Heon, L. Hultman, Y. Gogotsi, M.W. Barsoum, Two-dimensional nanocrystals produced by exfoliation of Ti₃AlC₂, *Adv. Mater.* 23 (2011) 4248–4253, <https://doi.org/10.1002/adma.201102306>.
- [50] Z. Liang, Y. Xue, Y. Guo, G. Zhang, H. Cui, J. Tian, Rationalizing and controlling the phase transformation of semi-metallic 1T'-phase and semi-conductive 2H-phase MoS₂ as cocatalysts for photocatalytic hydrogen evolution, *Chem. Eng. J.* 396 (2020), 125344, <https://doi.org/10.1016/j.cej.2020.125344>.
- [51] R. Dai, A. Zhang, Z. Pan, A.M. Al-Enizi, A.A. Elzatabry, L. Hu, G. Zheng, Epitaxial growth of lattice-mismatched core-shell TiO₂@MoS₂ for enhanced Lithium-ion storage, *Small* 12 (2016) 2792–2799, <https://doi.org/10.1002/sml.201600237>.
- [52] J. Tian, Z. Zhao, A. Kumar, R.I. Boughton, H. Liu, Recent progress in design, synthesis, and applications of one-dimensional TiO₂ nanostructured surface heterostructures: a review, *Chem. Soc. Rev.* 43 (2014) 6920–6937, <https://doi.org/10.1039/c4cs00180j>.
- [53] V. Schier, H.-J. Michel, J. Halbritter, ARXPS-analysis of sputtered TiC, SiC and Ti_{0.5}Si_{0.5}C layers, *Fresenius J. Anal. Chem.* 346 (1993) 227–232, <https://doi.org/10.1007/BF00321420>.
- [54] S. Myhraa, J.A.A. Crossley, M.W. Barsoum, Crystal-chemistry of the Ti₃AlC₂ and Ti₄AlN₃ layered carbide nitride phases—characterization by XPS, *J. Phys. Chem. Solids* 62 (2000) 811–817, [https://doi.org/10.1016/S0022-3697\(00\)00268-7](https://doi.org/10.1016/S0022-3697(00)00268-7).
- [55] J. Halim, K.M. Cook, M. Naguib, P. Eklund, Y. Gogotsi, J. Rosen, M.W. Barsoum, X-ray photoelectron spectroscopy of select multi-layered transition metal carbides (MXenes), *Appl. Surf. Sci.* 362 (2016) 406–417, <https://doi.org/10.1016/j.apusc.2015.11.089>.
- [56] T. Sultana, G.L. Georgiev, G. Auner, G. Newaz, H.J. Herfurth, R. Patwa, XPS analysis of laser transmission micro-joint between poly (vinylidene fluoride) and titanium, *Appl. Surf. Sci.* 255 (2008) 2569–2573, <https://doi.org/10.1016/j.apusc.2008.07.149>.
- [57] P.M. Jayaweera, E.L. Quah, H. Idriss, Photoreaction of ethanol on TiO₂ (110) single-crystal surface, *J. Phys. Chem. C* 111 (2007) 1764–1769, <https://doi.org/10.1021/jp0657538>.
- [58] J. Low, L. Zhang, T. Tong, B. Shen, J. Yu, TiO₂/MXene Ti₃C₂ composite with excellent photocatalytic CO₂ reduction activity, *J. Catal.* 361 (2018) 255–266, <https://doi.org/10.1016/j.jcat.2018.03.009>.
- [59] M.A. Lukowski, A.S. Daniel, F. Meng, A. Forticaux, L. Li, S. Jin, Enhanced hydrogen evolution catalysis from chemically exfoliated metallic MoS₂ nanosheets, *J. Am. Chem. Soc.* 135 (2013) 10274–10277, <https://doi.org/10.1021/ja404523s>.
- [60] W. Zhou, Z. Yin, Y. Du, X. Huang, Z. Zeng, Z. Fan, H. Liu, J. Wang, H. Zhang, Synthesis of few-layer MoS₂ nanosheet-coated TiO₂ nanobelt heterostructures for enhanced photocatalytic activities, *Small* 9 (2013) 140–147, <https://doi.org/10.1002/sml.201201161>.
- [61] Q. Liu, Q. Fang, W. Chu, Y. Wan, X. Li, W. Xu, M. Habib, S. Tao, Y. Zhou, D. Liu, T. Xiang, A. Khalil, X. Wu, M. Chhowalla, P.M. Ajayan, L. Song, Electron-doped 1T-MoS₂ via interface engineering for enhanced electrocatalytic hydrogen evolution, *Chem. Mater.* 29 (2017) 4738–4744, <https://doi.org/10.1021/acs.chemmater.7b00446>.
- [62] J. Han, X. Ji, X. Ren, G. Cui, L. Li, F. Xie, H. Wang, B. Li, X. Sun, MoO₃ nanosheets for efficient electrocatalytic N₂ fixation to NH₃, *J. Mater. Chem. A* 6 (2018) 12974–12977, <https://doi.org/10.1039/C8TA03974G>.
- [63] F. Gong, S. Ye, M. Liu, J. Zhang, L. Gong, G. Zeng, E. Meng, P. Su, K. Xie, Y. Zhang, Jian Liu, Boosting electrochemical oxygen evolution over yolk-shell structured O-MoS₂ nanoreactors with sulfur vacancy and decorated Pt nanoparticles, *Nano Energy* 78 (2020), 105284, <https://doi.org/10.1016/j.nanoen.2020.105284>.
- [64] H. Liu, Y. Zhang, J. Luo, The removal of inevitable NO_x species in catalysts and the selection of appropriate membrane for measuring electrocatalytic ammonia synthesis accurately, *J. Energy Chem.* 49 (2020) 51–58, <https://doi.org/10.1016/j.jechem.2020.01.029>.
- [65] C. Chen, Y. Liu, Y. Yao, Ammonia synthesis via electrochemical nitrogen reduction reaction on iron molybdate under ambient conditions, *Eur. J. Inorg. Chem.* 34 (2020) 3236–3241, <https://doi.org/10.1002/ejic.202000554>.
- [66] Y. Du, Z. He, F. Ma, Y. Jiang, J. Wan, G. Wu, Y. Liu, Anionic biopolymer assisted preparation of MoO₃@C heterostructure nanoparticles with oxygen vacancies for ambient electrocatalytic ammonia synthesis, *Inorg. Chem.* 60 (2021) 4116–4123, <https://doi.org/10.1021/acs.inorgchem.1c00218>.
- [67] Y.X. Luo, W.B. Qiu, R.P. Liang, X.H. Xia, J.D. Qiu, Mo-doped FeP nanospheres for artificial nitrogen fixation, *ACS Appl. Mater. Interfaces* 12 (2020) 17452–17458, <https://doi.org/10.1021/acsami.0c00011>.
- [68] G. Chen, M. Ding, K. Zhang, Z. Shen, Y. Wang, J. Ma, A. Wang, Y. Li, H. Xu, Single-atomic ruthenium active sites on Ti₃C₂ MXene with oxygen-terminated surface synchronize enhanced activity and selectivity for electrocatalytic nitrogen reduction to ammonia, *ChemSusChem* 15 (2022), e202102352, <https://doi.org/10.1002/cssc.202102352>.
- [69] Q. Li, T. Song, Z. Wang, X. Wang, X. Zhou, Q. Wang, Y. Yang, A general strategy toward metal sulfide nanoparticles confined in a sulfur-doped Ti₃C₂T_x MXene 3D porous aerogel for efficient ambient N₂ electroreduction, *Small* 17 (2021) 2103305, <https://doi.org/10.1002/sml.202103305>.
- [70] X. Xu, B. Sun, Z. Liang, H. Cui, J. Tian, High-performance electrocatalytic conversion of N₂ to NH₃ using 1T-MoS₂ anchored on Ti₃C₂ MXene under ambient conditions, *ACS Appl. Mater. Interfaces* 12 (2020) 26060–26067, <https://doi.org/10.1021/acsami.0c06744>.
- [71] W. Peng, M. Luo, X. Xu, K. Jiang, M. Peng, D. Chen, T. Chan, Y. Tan, Spontaneous atomic ruthenium doping in Mo₂CT_x MXene defects enhances electrocatalytic activity for the nitrogen reduction reaction, *Adv. Energy Mater.* 10 (2020) 2001364, <https://doi.org/10.1002/aenm.202001364>.
- [72] K. Chu, Y. Luo, P. Shen, X. Li, Q. Li, Y. Guo, Unveiling the synergy of O-vacancy and heterostructure over MoO_{3-x}/MXene for N₂ electroreduction to NH₃, *Adv. Energy Mater.* 12 (2022) 2103022, <https://doi.org/10.1002/aenm.202103022>.